An electromechanical material testing system for *in situ* electron microscopy and applications

Yong Zhu and Horacio D. Espinosa*

Department of Mechanical Engineering, Northwestern University, 2145 Sheridan Road, Evanston, IL 60208

Communicated by Zdenek P. Bazant, Northwestern University, Evanston, IL, August 2, 2005 (received for review April 8, 2005)

We report the development of a material testing system for *in situ* electron microscopy (EM) mechanical testing of nanostructures. The testing system consists of an actuator and a load sensor fabricated by means of surface micromachining. This previously undescribed nanoscale material testing system makes possible continuous observation of the specimen deformation and failure with subnanometer resolution, while simultaneously measuring the applied load electronically with nanonewton resolution. This achievement was made possible by the integration of electromechanical and thermomechanical components based on microelectromechanical system technology. The system capabilities are demonstrated by the *in situ* EM testing of free-standing polysilicon films, metallic nanowires, and carbon nanotubes. In particular, a previously undescribed real-time instrumented *in situ* transmission EM observation of carbon nanotubes failure under tensile load is presented here.

carbon nanotube | microelectromechanical system | nanomechanics | nanowires

Nanomechanical characterization of materials has recently attracted significant attention because of the emergence of various novel nanoscale materials and structures over the past decade. Nanotubes (1, 2) and nanowires (3) have shown great potential in a broad range of applications from nanocomposite nanoelectronics to nanoelectromechanical systems. These nanostructures have presented new challenges for the mechanics community concerning the identification of their properties and deformation mechanisms.

To achieve this goal, quantitative *in situ* mechanical testing of these structures by SEM, transmission EM (TEM), and scanning probe microscopes is essential. Progress in this area has been hindered by the lack of miniaturized material testing systems with adequate load and displacement accuracy. Existing measurement techniques can be categorized as follows:

- Techniques that measure load and displacement but cannot image the specimen during loading, e.g., force spectroscopy atomic force microscopy (4), nanoindentation (5), and on-chip testing (6, 7);
- Techniques that image the specimen in real time but cannot measure load and deformation independently (8, 9);
- Techniques that measure load and locally image deformation and failure by atomic force microscopy (10) or by optical interferometry (11), although the resolution is somewhat limited for the study of nanostructures; and
- Techniques that can image defects and measure load and deformation but that require frequent switching of the electron beam, between specimen and a deflecting beam used as load sensor, during which local deformation events may go unobserved (12–14).

Therefore, advances in nanomechanical testing require a new material testing system with the capability to independently apply and measure load without the need of imaging, e.g., electronically, while exhibiting adequate resolution for nanostructure testing. In this manner, the imaging can be used exclusively for real-time continuous observation of the specimen at the desired magnification. In this work, we demonstrate a previously undescribed microelectromechanical system (MEMS) that accomplishes this goal. The device includes an actuator (electromechanical or thermomechanical) and a load sensor based on capacitance measurement. The specimens can be thin films, 1D nanostructures, and biological structures. Thin films are cofabricated with the actuator and load sensor, while the nanostructures and biostructures can be placed across a gap between the actuator and the load sensor by a nanomanipulator (15, 16) or guided self-assembly (17). Because of its small size, the MEMS device is well suited for *in situ* testing of nanostructures inside SEM, TEM, scanning probe microscopes, and x-ray synchrotron stages.

Device Design, Fabrication, and Calibration

Two types of actuators can be used in the device design: comb drive electrostatic actuator and in-plane thermal actuator. The comb drive actuator is force controlled (6), whereas the thermal actuator is displacement controlled, i.e., it prescribes the displacement to the specimen on a given supplied voltage.

For a description of the principle of the comb drive actuator, see ref. 18. Here, we briefly describe the thermal actuator, which can deliver a large force (up to tens of millinewtons) and a moderate displacement (up to tens of micrometers) (see Fig. 1*a*). It consists of inclined freestanding beams connected to a shuttle at one end and fixed to the substrate at the other end. When a voltage is applied across the inclined beams (V-shaped beams), the current flux causes joule-heating and thermal expansion. Because of the inclined configuration of the beams, the shuttle is pushed forward. In free motion (without connection to the specimen), the thermal actuator displacement is given as

$$U^{\Delta T} = \alpha \Delta T l \frac{\sin\theta}{\left(\sin^2\theta + \cos^2\theta \frac{12I}{Al^2}\right)}, \qquad [1]$$

where α is the thermal expansion coefficient of the beam material, ΔT is the average temperature change in the inclined beams, l is the beam length, I is the moment of inertia of one beam in the plane parallel to the substrate ($= (1/12)Eb^3h$), E is the Young's modulus of the actuator material, b is the beam width, h is the beam height, A is the cross-sectional area of a beam, and θ is the angle between the beams and the transverse direction to the shuttle motion. Additional details of the design and operation of the thermal actuator are described by Y.Z. *et al.* (Y.Z., A. Corigliano, and H.D.E., unpublished data).

The load sensor integrated in the testing platform is similar to the MEMS accelerometer (Analog Devices, Norwood, MA) in that they are both based on differential capacitive sensing and fabricated by surface micromachining. The load sensor consists

Abbreviations: EBID, electron beam-induced deposition; FIB, focused ion beam; MWCNT, multiwalled carbon nanotube; MEMS, microelectromechanical system; TEM, transmission EM.

*To whom correspondence should be addressed. E-mail: espinosa@northwestern.edu.

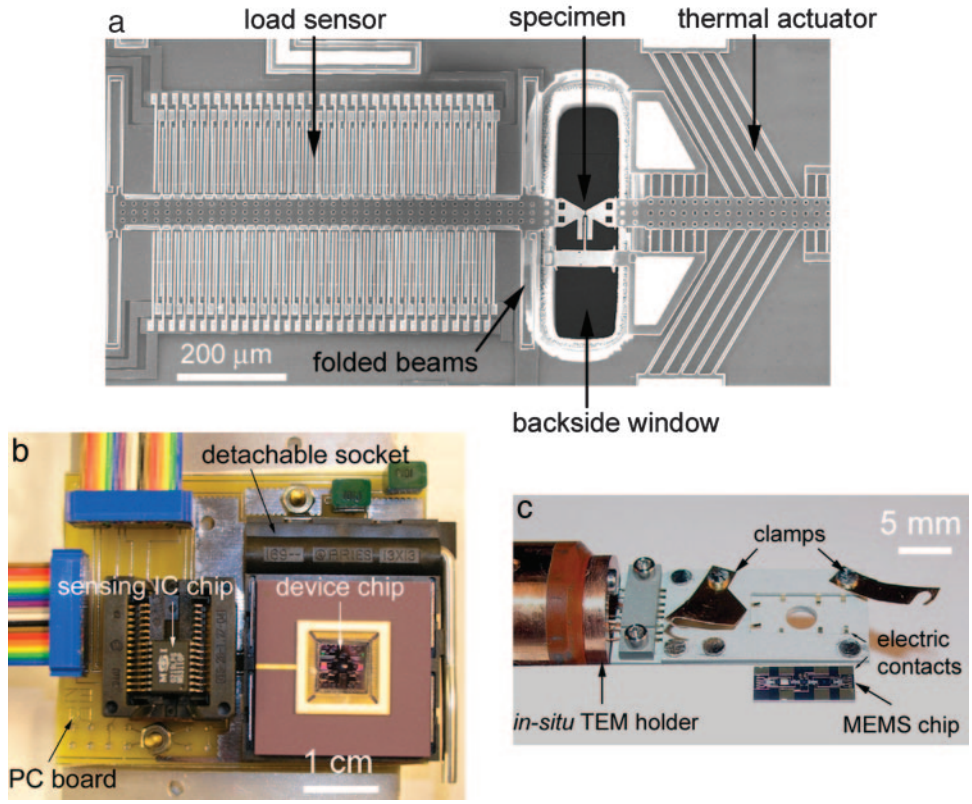

Fig. 1. *In situ* SEM and TEM tensile testing device including actuator, load sensor, and specimen. Four folded beams support the load sensor. (*a*) Testing device used in *in situ* TEM. (*b*) Experimental setup for *in situ* SEM testing. MEMS device chip is positioned near the MS3110 chip on a printed circuit board. The setup is connected to a power supply, a digital multimeter, and a computer outside the SEM by means of a chamber feedthrough. (*c*) *In situ* TEM holder (containing a feedthrough and eight electric contact pads) along with a 5 × 10 mm MEMS chip. In an actual experiment, the MEMS chip is flipped, placed in the TEM holder, and fixed by the left and right clamps.

of a rigid shuttle with one set of movable fingers and two sets of stationary fingers. A lumped model of the sensor consists of two capacitors in series. Shuttle displacement causes increase of one capacitance and decrease of the other. Within a moderate displacement range, the capacitance change is proportional to the displacement, namely

$$\Delta C = C_1 - C_2 = N\varepsilon A\left(\frac{1}{d_0 - \Delta d} - \frac{1}{d_0 + \Delta d}\right) \approx \frac{2N\varepsilon A}{d_0^2}\Delta d, \quad [2]$$

where ε is the electric permittivity, N the number of units of differential capacitors, A and d_0 are the overlap area and initial gap between the movable finger and each stationary finger, respectively, and Δd the displacement of the load sensor. The load sensor is anchored to the substrate by four folded beams that are designed with a range of stiffness for testing various materials of interest. For a discussion of stiffness selection and a lumped model of the device, see ref. 19.

The devices are fabricated at a commercial foundry (MEMSCAP, Durham, NC) by using the multi-user MEMS process. In our design for *in situ* SEM testing, 20 devices with different types of actuators and load sensors are arranged in a 10×10 mm^2 chip. To achieve electrical connection, there are 100 gold pads fabricated in the same chip around the periphery. The chip is glued to the cavity of a ceramic pin grid array package, and the gold pads are wire-bonded to the 100 leads around the cavity, as shown in Fig. 1*b*. Corresponding pins in the back of the package make the electric connection to an outer circuit, which in turn is connected to electronic actuation and measuring instrumentation.

Measuring capacitance changes with subfemtofarad resolution, as required in this application, is quite challenging. Fortunately, a charge-sensing measuring circuit that can mitigate the effect of parasitic capacitance has been developed by the MEMS community (20). A commercially available integrated circuit based on this method, Universal Capacitive Readout MS3110 (MicroSensors, Costa Mesa, CA), is used here. The MEMS device chip is positioned very close to the sensing integrated circuit chip (MS3110) to minimize the stray capacitance and electromagnetic interference (Fig. 1*b*). The output voltage is proportional to the capacitance change.

In addition to the *in situ* SEM measurements reported here, this device has the potential to impact other nanoscale characterization techniques. For instance, *in situ* TEM testing of nanostructures is achievable by microfabrication of a window under the specimen area. The major challenge is to etch such a window, from the back of the silicon wafer, without damaging the previously fabricated structures. We have accomplished such a task by deep reactive ion etching of the window before device release. Details of the fabrication process are described elsewhere (H.D.E., Y.Z., and N. Moldovan, unpublished data). Fig. 1*c* shows a MEMS chip (5×10 mm) containing four MEMS devices. The two devices in the center can be used to perform *in situ* TEM testing, and the other two devices can be used in calibration tests. The chip has eight contact pads for electric actuation/sensing. Fig. 1*a* is a magnified view of one such device. The backside window, with dimensions of 130×400 μm, is clearly visible. The chip is designed to be directly mounted on a specially designed TEM holder containing a feed-through and interconnects to address electrically the devices (Fig. 1*c*). In this

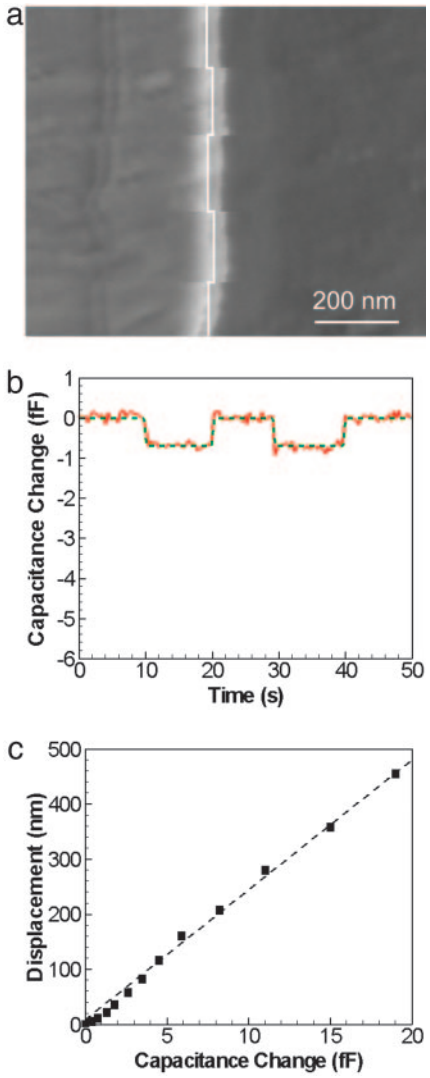

Fig. 2. Calibration of the load sensor showing the relationship between capacitance change and measured displacement from SEM images at a series of actuation voltages. (*a* and *b*) Signatures when actuator is at 2 V; reference feature in the SEM image showing a motion of 15 nm due to four ON–OFF actuations (*a*) and plot corresponding to a 0.7 fF capacitance change resulting from the same actuation (*b*). Both raw data and fitted data are shown in the plot of capacitance measurements. (*c*) Plot of displacement vs. capacitance change resulting from the calibration.

case, the sensing integrated circuit chip (MS3110) used in the capacitance measurement is located outside of the TEM.

Calibration of the displacement, capacitance change relation for the load sensor, is described in ref. 15. Here, we report a more accurate version. A particular feature in the movable shuttle is selected as reference in the SEM image. The device is actuated ON and OFF sequentially four times during the SEM scan. The feature corresponding to the ON–OFF actuation cycles is captured in the SEM image (Fig. 2*a*), and simultaneously the capacitance change is recorded (Fig. 2*b*). Fig. 2*c* correlates the displacement (load) and the capacitance change. It follows a linear relationship, which agrees well with Eq. **2**. The resolution of the measured capacitance change is 0.05 fF, and the corresponding displacement resolution is 1 nm. For a load sensor with stiffness of 11.8 N/m, designed for testing carbon nanotubes and nanowires, the load resolution is 12 nN, which is quite adequate (12, 15). Depending on the application, the load resolution can be increased to ≈1 nN by decreasing the sensor stiffness. Additional details on the load sensor calibration can be found in ref. 15.

Applications

The testing system shown in Fig. 1 was used to test three types of structures: freestanding polySi films and palladium nanowires inside an SEM and carbon nanotubes inside a TEM.

For the testing of freestanding thin films, polySi was selected because of its well-characterized Young's modulus and failure strength (11) and ease of cofabrication with the device. Because the minimum feature size by standard photolithography is ≈2 μm, the cofabricated polySi specimen was further nanomachined by focused ion beam (FIB) to reduce the sample minimum dimension to 350–450 nm. A dog-bone-shaped polySi specimen with a trapezoidal cross-section was obtained (Fig. 3*a*). Two platinum (Pt) lines (with a spacing of 2.5 μm) were deposited by electron beam-induced deposition (EBID) (12, 16) in a dual-beam FIB/SEM instrument (FEI, Hillsboro, OR) for deformation measurement (Fig. 3*b*). Quantification of length increase between these two marks was done by means of image analysis with edge detection software. Two specimens were tested, resulting in the stress–strain curves shown in Fig. 3*c*. The specimens exhibit nearly the same Young's modulus of 155 ± 5 GPa and failure strengths of 0.7 and 1.42 GPa. The results are consistent with the values reported for multi-user MEMS process polySi thin films (11). The variation in measured failure strength is to be expected in view of the weakest link theory (Weibull statistics) applicable to brittle materials (21). Examination of the failure surface (Fig. 3*d*) reveals a mirror region at the top right corner of the fracture surface, which is typical of brittle fracture initiation (7, 10, 11).

For the testing of nanowires, palladium (Pd) nanowires were synthesized by using a porous alumina membrane as template (22). The tested nanowires were ≈20–30 μm long and 200 nm in diameter. They were polycrystalline with average grain size of ≈20 nm. To mount a single nanowire (specimen) onto the device, nanomanipulation was used consisting of the following steps: (*i*) nanowire dispersion in isoproponal by ultrasonication for 30 min; (*ii*) deposition of nanowire suspension on top of a TEM grid with a micropipette; (*iii*) manipulation of a protruding nanowire from grid edge; and (*iv*) mounting of the nanowire between the actuator and the load sensor. The last two steps were performed inside the same dual-beam FIB/SEM instrument. EBID of Pt was used for nanowelding. A nanomanipulator possessing 1-nm resolution in three orthogonal axes (Klocke Nanotechnik, Aachen, Germany) was used to pick up a protruding nanowire. After welding the nanowire to the tungsten tip of the manipulator, FIB was used to cut the nanowire and release it from the other end. Through *x*, *y*, and *z* motion of the manipulator, the nanowire was brought close to the MEMS device (Fig. 4*a*). Contact was confirmed by electron beam and ion beam imaging through two different views. The free end in contact with the actuator shuttle was then welded (Fig. 4*b*). After that, FIB was used to cut the nanowire such that the other end was freed (Fig. 4*c*). The manipulator tip then was used to push down this free end until it made contact with the sensor shuttle. It then was EBID nanowelded (Fig. 4*d*). Through this procedure, nanowires were successfully mounted on the devices.

A particular Pd nanowire was tested *in situ* the FIB/SEM. The length between the two welding locations was measured to be 3 ± 0.2 μm. The gap edges (2 μm apart) were used as displacement markers. Assuming no sliding between the nanowire and the two welded ends, the gap size increase during tensile testing was considered as the nanowire elongation. Quantification of the gap increase was done by means of image analysis with

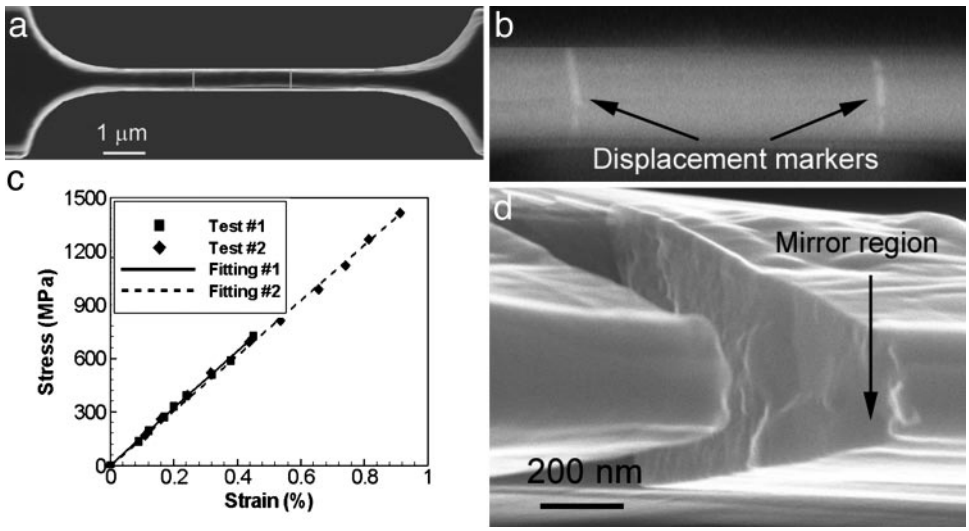

Fig. 3. Quantitative *in situ* SEM test of a freestanding polySi film. (*a*) Dog-bone-shaped tensile test specimen. (*b*) Magnified view of two Pt displacement markers deposited by EBID. (*c*) Stress–strain curves of two *in situ* SEM tests. Both specimens were 6 μm long and 1.6 μm thick. One had a top width of 0.34 μm and bottom width of 0.87 μm, whereas the other had a top width of 0.42 μm and bottom width of 1.04 μm. (*d*) Fracture surface of polySi beam showing a mirror region indicative of brittle fracture initiation.

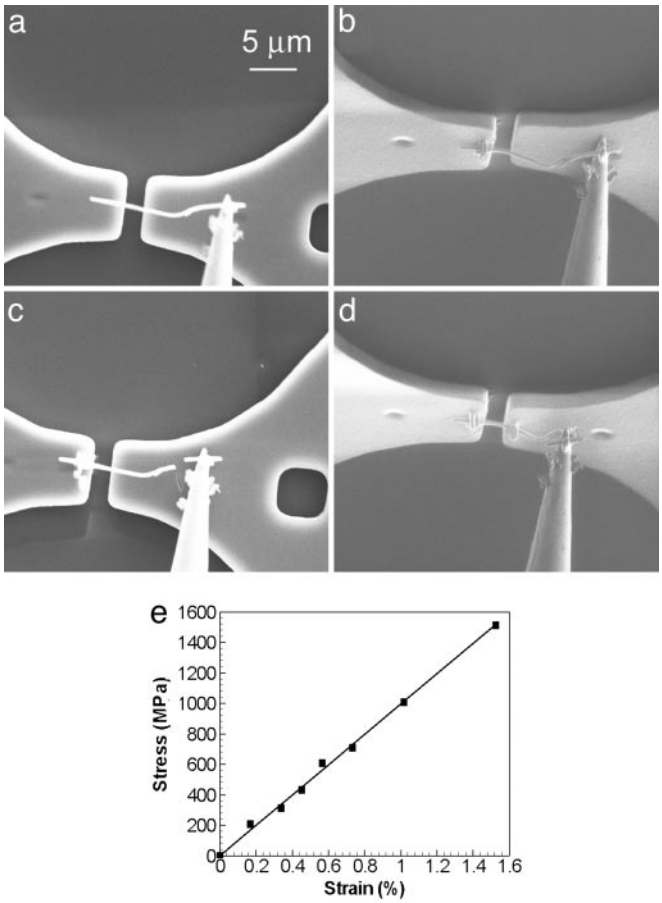

Fig. 4. Nanomanipulation procedure to mount a Pd nanowire in the MEMS and test results. (*a*) Approach and contact the nanowire to the MEMS device. (*b*) Weld one end of the nanowire to the actuator shuttle using EBID of Pt gas precursor. (*c*) Cut the other end using FIB. (*d*) Weld the free end to the load sensor shuttle. (e) Stress–strain curve of a Pd nanowire exhibiting a Young's modulus of 99.4 ± 6.6 GPa and a strength higher than its bulk counterpart. *a* and *c* are SEM images; *b* and *d* are FIB images. There is a 52° view angle difference between SEM and FIB.

edge detection software. Hence, strain was computed as the ratio between gap size increase and distance between welding points. The stress–strain curve recorded during the experiment is plotted in Fig. 4*e*. It is observed that the measured Young's modulus was 99.4 ± 6.6 GPa, which is ≈20–30% lower than that of a polycrystalline Pd and in between the maximum and minimum values for single-crystalline Pd as a function of the crystal orientation. For single-crystalline Pd, the Young's modulus in the ⟨111⟩ direction is 191.5 GPa, in the ⟨100⟩ direction is 73.4 GPa, and in the ⟨110⟩ direction is 136.5 GPa (23). Young's modulus of polycrystalline Pd is 132 GPa (24). There was an ≈5° misalignment between the axial direction of the nanowire and the stretching direction, which caused <1% error of the Young's modulus. Reduction in the value of Young's modulus with respect to the bulk value has been observed in nanocrystalline materials. Grain boundary compliance and creep are attributed to this phenomenon (14, 24). Another feature revealed by the test is that the nanowire remained elastic and did not fracture up to an applied stress of 1.5 GPa. This value is much higher than the yield stress of nanocrystalline Pd in bulk form (25). This finding confirms that when the material scales down, its strength increases and tends to approach the theoretical strength of the material (≈1/10 of the Young's modulus) (25). This phenomenon can be attributed to absence of defects in the material atomic structure and the high stress threshold for the nucleation of defects (26, 27). Because the tested nanowire turned out to be much stronger than anticipated, the MEMS device designed with a relatively low load sensor stiffness was not able to break it within the range of admissible actuator voltages.

Multiwalled carbon nanotubes (MWCNTs) were tested *in situ* the TEM (JEOL 2010F, 200kV accelerating voltage). The specimens were mounted on the device by following the manipulation procedure described above. A particular MWCNT was tested inside a TEM by using the holder shown in Fig. 1*a*. Its outer diameter was ≈130 nm and inner diameter was 99 nm, as shown in Fig. 5*a*. The length between the two welding locations was 2.57 ± 0.2 μm. The specimen was progressively loaded, and its deformation was continuously monitored. A movie showing the deformation of the MWCNT under tension until fracture is available from the authors upon request. A fracture strength of 15.84 GPa and a failure strain of 1.56% was measured. These results are in agreement with

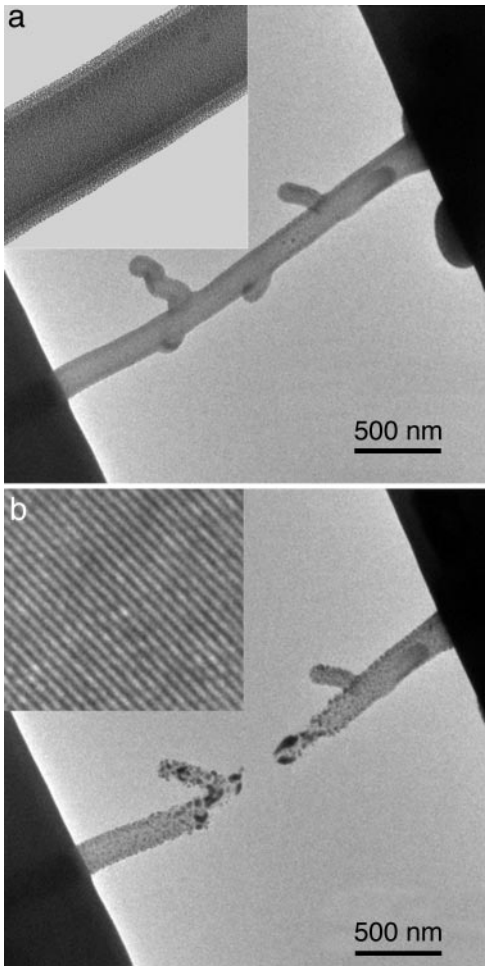

Fig. 5. *In situ* TEM tensile test of an MWCNT. (*a*) TEM image before the test. *Inset* shows the multiple graphite shells. The MWCNT has outer diameter of 130 nm and inner diameter of 99 nm. (*b*) TEM image after the test. Post-failure crystallization is clearly seen. *Inset* is a high-resolution TEM image of a particular nanograin at the fracture region showing that the grain is single crystalline. The three tiny tubes attached to the main tube were present during nanomanipulation when the MWCNT specimen was taken out from a bundle. The procedure for specimen attachment to the MEMS testing system was the same to the one used in the testing of the Pd nanowire.

those reported in ref. 12. However, a previously undescribed phenomenon was observed during the *in situ* experiment. After failure, the graphite shell atomic structure disappeared. Instead, a large number of nanoparticles (with diameters ranging from 5 to 50 nm) embedded in an amorphous matrix were observed (see Fig. 5*b*). Both high-resolution TEM and nanodiffraction confirmed that the nanoparticles are single-crystal Pt. We therefore conclude that a thin layer of amorphous Pt coated the MWCNT during EBID and that this Pt layer transformed to a crystalline phase during the straining and failure of the MWCNT. Furthermore, electron energy loss spectroscopy analysis revealed that the amorphous matrix is made of carbon. It is therefore inferred that the crystalline structure of the carbon nanotubes (graphite sheets) transformed to amorphous carbon upon failure.

Discussion

As shown by the above tests, the MEMS-based material testing system with integrated electronic load application and sensing greatly enhances the instrumentation capabilities for *in situ* atomic force microscopy, SEM, and TEM testing of nanostructures. With this system, microscopy can be focused on capturing deformation mechanism while the corresponding load history is recorded electronically. Note that addition of a second differential capacitor sensor on the actuator side of the sample would directly provide an electronic measurement of average specimen elongation (H.D.E., Y.Z., and N. Moldevan, unpublished data). In such a case, both load and average deformation would be measured electronically. Furthermore, the MEMS-based material testing system potentially can be applied to characterize the mechanical and electromechanical properties not only of nanowires and nanotubes but also of a large number of organic materials, including DNA, proteins, and nanofibers (4).

Although the developed device has been discussed in the context of *in situ* SEM and TEM tensile testing, a large number of related applications are envisioned. To cite just one, let us highlight its applicability to *in situ* TEM nanoindentation experiments. Quantitative *in situ* nanoindentation in TEM has provided useful insight in the study of dislocation nucleation and propagation (28). In the experiments reported in ref. 28, the load–displacement relation was derived from the indenter motion. However, such information cannot be obtained in the case of dark-field TEM that is generally used in studying the effect of crystallography. In the dark-field condition, the image is formed by using a strongly diffracted electron beam from one grain only. Our MEMS-based material testing system with electronic load sensing can in principle be used to overcome this limitation. A low aspect ratio carbon nanotube or nanowire mounted on the actuator side, following a nanomanipulation procedure similar to that described above, would constitute the indenter. As a matter of fact, carbon nanotubes have been widely used as tips for high-resolution atomic force microscopy (29). Clearly, the V-shape of the actuator needs to be inverted such that the displacement vector produced by the actuator is in the direction of the specimen-load sensor.

We thank H. H. Wang (Argonne National Laboratory, Argonne, IL) and C. Y. Han (Argonne National Laboratory) for providing the nanowires; I. Petrov, E. Olson, and J.-G. Wen for facilitating the *in situ* TEM holder shown in Fig. 1*c*; B. Peng for assistance in the nanomanipulation; and C. Li and N. Zaluzec for assistance in the *in situ* TEM experiments. This work was supported by National Science Foundation Grant DMR-0315561. Nanomanipulation was carried out in the Center for Microanalysis of Materials at the University of Illinois, which is partly supported by the U.S. Department of Energy under Grant DEFG02-96-ER45439.

1. Iijima, S. (1991) *Nature* **354,** 56–58.
2. Fennimore, A. M., Yuzvinsky, T. D., Han, W. Q., Fuhrer, M. S., Cumings, J. & Zettl, A. (2003) *Nature* **424,** 408–410.
3. Cui, Y. & Lieber, C. M. (2001) *Science* **291,** 851–853.
4. Marszalek, P. E., Greenleaf, W. J., Li, H., Oberhauser, A. F. & Fernandez, J. M. (2000) *Proc. Natl. Acad. Sci. USA* **97,** 6282–6286.
5. Oliver, W. C. & Pharr, G. M. (1992) *J. Mater. Res.* **7,** 1564.
6. Saif, M. T. A. & MacDonald. (1996) *Sens. Actuators A* **52,** 65–75.
7. Kahn, H., Ballarini, R., Mullen, R. L. & Heuer, A. H. (1999) *Proc. R. Soc. London A* **455,** 3807–3823.
8. Hugo, R. C., Kung, H., Weertman, J. R., Mitra, R., Knapp, J. A. & Follstaedt, D. M. (2003) *Acta Materialia* **51,** 1937–1943.
9. Ke, M., Hackney, S. A., Milligan, W. W. & Aifantis, E. C. (1995) *Nanostruct. Mater.* **5,** 689–698.
10. Chasiotis, I. & Knauss, W. G. (2003) *J. Mech. Phys. Solids* **51,** 1533–1550.
11. Sharpe, W. N., Jr., Jackson, K. M. Hemker, K. J. & Xie, Z. (2001) *J. Microelectromech. Syst.* **10,** 317–326.
12. Yu, M. F., Lourie, O., Dyer, M. J., Moloni, K., Kelly, T. F. & Ruoff, R. S. (2000) *Science* **287,** 637–640.
13. Haque, M. A. & Saif, M. T. A. (2002) *Exp. Mech.* **42,** 123–128.
14. Haque, M. A. & Saif, M. T. A. (2004) *Proc. Natl. Acad. Sci. USA* **101,** 6335–6340.
15. Zhu, Y., Moldovan, N. & Espinosa, H. D. (2005) *Appl. Phys. Lett.* **86,** 013506.

16. Williams, P. A., Papadakis, S. J., Falvo, M. R., Patel, A. M., Sinclair, M., Seeger, A., Helser, A., Taylor, R. M., II, Washburn, S. & Superfine, R. (2002) *Appl. Phys. Lett.* **80,** 2574–2576.
17. Kong, J., Soh, H. T., Cassell, A., Quate, C. F. & Dai, H. (1998) *Nature* **395,** 878–881.
18. Tang, W. C., Ngugen, T-C. & Howe, R. T. (1992) *Sens. Actuators A* **21,** 328–331.
19. Prorok, B. C., Zhu, Y., Espinosa, H. D., Guo. Z., Bazant, Z. P., Zhao, Y. & Yakobson, B. I. (2004) in *Encyclopedia of Nanoscience and Nanotechnology*, ed. Nalwa, H. S. (American Scientific, Stevenson Ranch, CA), pp. 555–600.
20. Senturia, S. D. (2002) *Microsystem Design* (Kluwer Academic, Boston).
21. Greek, S., Ericson, F., Johansson, S. & Schweitz, J. (1997) *Thin Solid Films* **292,** 247–254.
22. Xiao, Z. L., Han, C. Y., Welp, U., Wang, H. H., Kwok, W. K., Willing, G. A., Hiller, J. M., Cook, R. E., Miller, D. J. & Crabtree, G. W. (2002) *Nano Lett.* **2**, 1293–1297.
23. Simmons, G. & Wang, H. (1971) *Single Crystal Elastic Constants and Calculated Aggregate Properties: A Handbook* (MIT Press, Cambridge, MA).
24. Sakei, S. Tanimoto, H. & Mizubayshi, H. (1999) *Acta Mater.* **47,** 211–217.
25. Courtney, T. H. (2000) *Mechanical Behavior of Materials* (McGraw–Hill, Boston).
26. Espinosa, H. D., Prorok, B. C. & Peng, B. (2004) *J. Mech. Phys. Solids* **52,** 667–689.
27. Uchic, M. D., Dimiduk, D. M., Florando, J. N. & Nix, W. D. (2004) *Science* **305,** 986–989.
28. Minor, A. M., Morris, J. W., Jr., & Stach, E. A. (2001) *Appl. Phys. Lett.* **79**, 1625–1627.
29. Dai, H., Hafner, J. H., Rinzler, A. G., Colbert, D. T. & Smalley, R. E. (1996) *Nature* **384,** 52–54.